

Accelerating O-Redox Kinetics with Carbon Nanotubes for Stable Lithium-Rich Cathodes

Junhua Zhou, Zhujie Chen, Guo Yu, Keni Ma, Xueyu Lian, Shuo Li, Qitao Shi, Jiaqi Wang, Lingli Guo, Yu Liu, Alicja Bachmatiuk, Jingyu Sun, Ruizhi Yang, Jin-Ho Choi, and Mark H. Rummeli*

Lithium-rich cathodes (LRCs) show great potential to improve the energy density of commercial lithium-ion batteries owing to their cationic and anionic redox characteristics. Herein, a complete conductive network using carbon nanotubes (CNTs) additives to improve the poor kinetics of LRCs is fabricated. Ex situ X-ray photoelectron spectroscopy first demonstrates that the slope at a low potential and the following long platform can be assigned to the transition metal and oxygen redox, respectively. The combination of galvanostatic intermittent titration technique and electrochemical impedance spectroscopy further reveal that a battery with CNTs exhibited accelerated kinetics, especially for the O-redox process. Consequently, LRCs with CNTs exhibit a much better rate and cycling performance ($\approx 89\%$ capacity retention at 2 C for over 200 cycles) than the Super P case. Eventually, TEM results imply that the improved electrochemical performance of the CNTs case also benefits from its more stable bulk and surface structures. Such a facile conductive additive modification strategy also provides a universal approach for the enhancement of the electron diffusion properties of other electrode materials.

graphite materials).^[3] Both spinel-type (LiMn_2O_4 , $\approx 120 \text{ mAh g}^{-1}$) and polyanion-type (LiFePO_4 , $\approx 150 \text{ mAh g}^{-1}$) materials can take full advantage of the transition metal redox (one-electron transfer), whereas the large molecular mass limits their specific capacity.^[4] Layered materials, such as LiCoO_2 , can only partially utilize transition metal redox (less than one-electron transfer), as high-voltage charging causes severe structural deterioration.^[5] Although nascent nickel-rich cathodes ($\approx 200 \text{ mAh g}^{-1}$), such as $\text{LiNi}_{0.8}\text{Co}_{0.1}\text{Mn}_{0.1}\text{O}_2$ (NCM811) and $\text{LiNi}_{0.8}\text{Co}_{0.15}\text{Al}_{0.05}\text{O}_2$ (NCA), possess decent capacity by increasing the nickel content as the nickel redox can occur at a relatively low potential, there is little potential to further improve their capacity.^[6]


The LRCs, usually expressed as a $\text{Li}_2\text{MnO}_3 \cdot \text{LiNi}_x\text{Co}_y\text{Mn}_z\text{O}_2$ ($x + y + z = 1$) formula, possesses a superior specific capacity ($> 250 \text{ mAh g}^{-1}$) among cathode

materials, owing to its cationic redox ($\text{LiNi}_x\text{Co}_y\text{Mn}_z\text{O}_2$ part at relatively low potential, $< 4.5 \text{ V}$ versus Li/Li^+) and anionic redox (Li_2MnO_3 part at high potential, $4.5\text{--}4.8 \text{ V}$).^[7] Nevertheless, LRCs also present serious challenges, including high voltage hysteresis and low coulombic efficiency in the first cycle, high capacity and voltage fading during cycling, and poor rate performance.^[8–12] These problems primarily occur from irreversible

1. Introduction

Developing LIBs with continuously increasing energy densities is a core goal for material scientists to overcome anabolic energy and environmental crises.^[1,2] A real bottleneck lies in cathode materials, which have a lower capacity ($< 250 \text{ mAh g}^{-1}$) than the anode ($> 330 \text{ mAh g}^{-1}$ for commercial

J. Zhou, Z. Chen, G. Yu, K. Ma, X. Lian, S. Li, Q. Shi, J. Wang, L. Guo, Y. Liu, J. Sun, R. Yang, J.-H. Choi, M. H. Rummeli
College of Energy
Soochow Institute for Energy and Materials InnovationS (SIEMIS)
Key Laboratory of Advanced Carbon Materials and Wearable Energy
Technologies of Jiangsu Province
Soochow University
Suzhou 215006, P. R. China

 The ORCID identification number(s) for the author(s) of this article can be found under <https://doi.org/10.1002/smt.202200449>.

© 2022 The Authors. Small Methods published by Wiley-VCH GmbH. This is an open access article under the terms of the Creative Commons Attribution-NonCommercial License, which permits use, distribution and reproduction in any medium, provided the original work is properly cited and is not used for commercial purposes.

DOI: 10.1002/smt.202200449

A. Bachmatiuk
LUKASIEWICZ Research Network
PORT Polish Center for Technology Development
Stablowicka 147, 54-066 Wrocław, Poland

J. Sun
Beijing Graphene Institute (BGI)
Beijing 100095, P. R. China

M. H. Rummeli
Leibniz Institute for Solid State and Materials Research Dresden
P.O. Box 270116, D-01171 Dresden, Germany
E-mail: m.ruemmeli@ifw-dresden.de

M. H. Rummeli
Centre of Polymer and Carbon Materials
Polish Academy of Sciences
M. Curie-Skłodowskiej 34, 41-819 Zabrze, Poland

M. H. Rummeli
Institute of Environmental Technology
VSB-Technical University of Ostrava
17. Listopadu 15, 708 33 Ostrava, Czech Republic

anionic oxygen redox (O-redox) and the corresponding induced-surface structural reconstruction from the layer (C2/m) to spinel (Fd3m) and finally to the disordered rock-salt (Fm3m) phase.^[13–17]

The rate property of the fast-charging ability is crucial to enabling the popularization of electric vehicles. Strategies such as covering the surface carbon coating and bulk heteroatom doping have been applied to solve the poor kinetics of LRCs. For example, Cho et al. reported a novel surface treatment method with a few layers of reduced graphene oxide coating, and the produced LRCs exhibited superior rate and cycling performance because of its improved surface conductivity, inhibition of metal dissolution, and enhanced structural stability.^[18] Zhou et al. clearly observed improved rate performance of LRCs by bulk Sn doping because the large Sn⁴⁺ ion can expand the interlayer spacing of the (003) lattice plane without damaging the layer structure, resulting in accelerated Li⁺ diffusion.^[19]

However, complete surface carbon coating and pure phase doping are difficult with respect to the material preparation process, which is crucial for mass production. Herein, we propose a facile method by simply adding a small amount of CNTs as conductive additives during the slurry-making process, which

can greatly improve the electrochemical performance of the LRCs. The GITT and EIS revealed that the battery with CNTs exhibited accelerated kinetics, especially for the O-redox process. Consequently, an LRCs with CNTs exhibits a much better rate and cycling performance (~89% capacity retention at 2 C for over 200 cycles) than the SP case. TEM results imply that the improved electrochemical performance of the CNTs case also benefits from its more stable bulk and surface structures. Such a facile conductive additive modification strategy also provides a universal approach to enhancing the electron diffusion properties of other electrode materials, such as LiFePO₄, Si, and S.

2. Results and Discussion

2.1. Physical Characterization of LRCs and Conductive Additives

The most typical LRCs, Li₂MnO₃·LiNi_{1/3}Co_{1/3}Mn_{1/3}O₂ (Li_{1.2}Mn_{0.54}Ni_{0.13}Co_{0.13}O₂), was chosen as a model material to explore its O-redox nature. From the XRD patterns in **Figure 1a**, LRCs exhibited characteristic (003), (101), and (104) diffraction

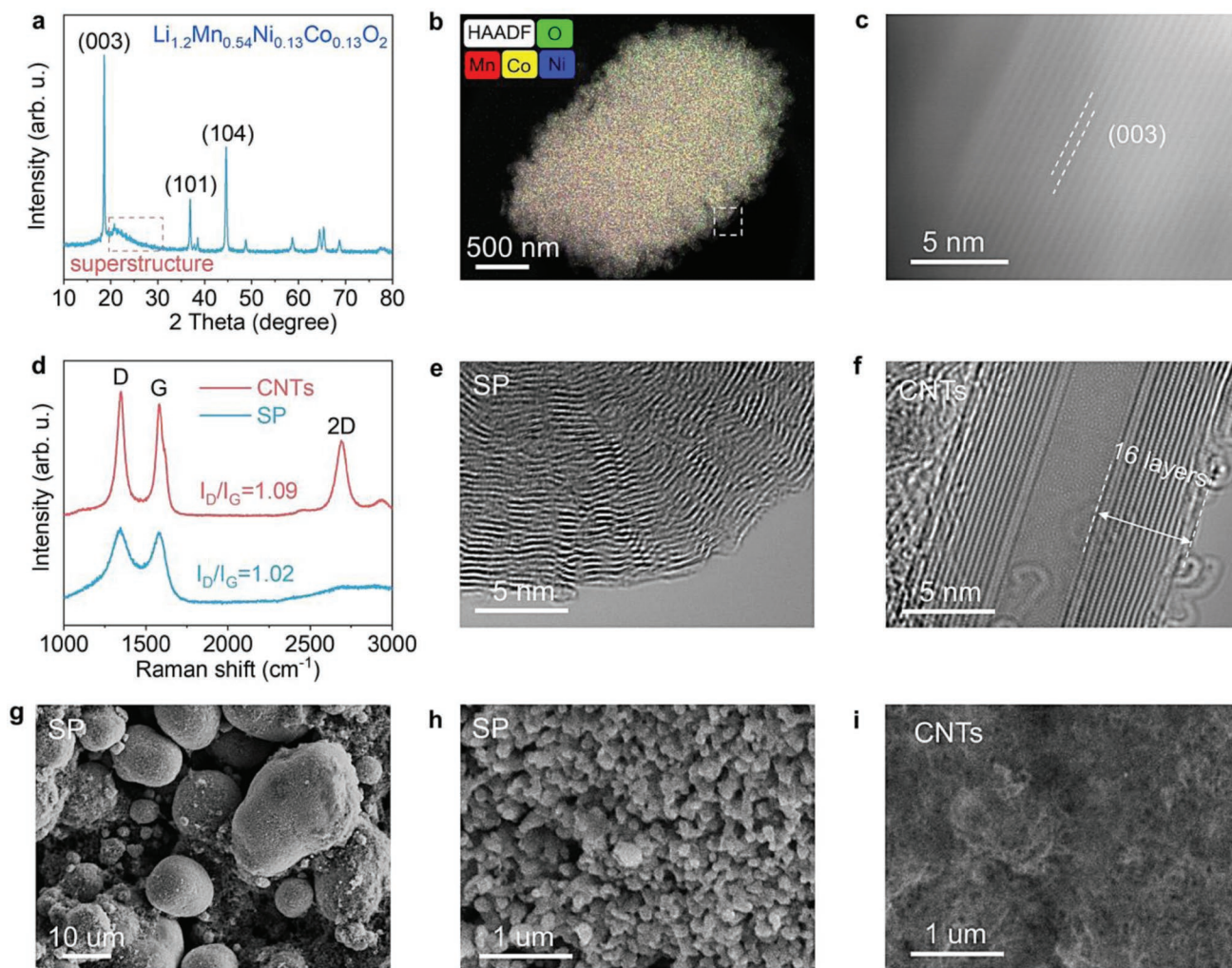


Figure 1. Physical characterization of LRCs and conductive additives. a–c) XRD patterns (a), EDS mapping (b), and HAADF-STEM images (c) of LRCs. d–f) Raman patterns (d), TEM images of SP (e) and CNTs (f). g–i) SEM images of LRCs electrode using SP (g, h) and CNTs (i) additives.

peaks with the C2/m space group.^[20] The weak Bragg peaks between 20° and 30°, marked with a rectangle in Figure 1a, can be indexed to the famous honeycomb-like superstructure composed of Li and transition metal atoms. In Figure 1b, high-angle annular dark-field-energy dispersive spectroscopy (HAADF-EDS) mapping shows the typical spherical-like morphology of LRCs, with a secondary particle size of approximately 3 μm, made up of smaller primary particles (≈100 nm). HAADF-EDS further exhibits the uniform distribution of Mn, Co, Ni, and O in the initial sample, and the absence of a Li signal owing to its low X-ray scattering ability. As seen in Figure 1c, HAADF-scanning transmission electron microscopy (STEM) images, which are also called Z-contrast images ($Z^{1.7}$), are very suitable for sample characterization with heavy atoms such as Ni, Co, and Mn. The HAADF-STEM images display the interlayer spacing of the LRCs along the *c*-axis of approximately 4.7 Å, assigned to the (003) lattice plane.

Super P (SP), a commonly used carbon conductive additive, was used for comparison with CNTs. The intensity ratio between D (1350 cm⁻¹) and G (1580 cm⁻¹) peaks (I_D/I_G) can be applied to judge the crystal quality of carbon, that is, the higher value, the lower crystallinity. From Figure 1d, the SP and CNTs show similar I_D/I_G values and very strong D peaks, indicating their defective character. Nevertheless, the CNTs exhibit much sharper (smaller full width at half maximum) D and G peaks than that of SP, demonstrating superior crystallinity. Meanwhile, the newly appeared 2D (2700 cm⁻¹) peak for the CNTs specimens is attributed the contribution of sp² C, *viz.*, better graphitization.^[21] High-resolution transmission electron microscopy (HRTEM) images (Figure 1e) show the curved lattice plane of SP with a particle size of approximately 20 nm (Figure S2b, Supporting Information), in agreement with its low-crystalline nature. The CNTs in Figure 1f exhibit multilayer (16 layers) characteristics with a length of approximately 50 μm.

The LRCs electrode with SP or CNTs conductive additives was prepared using a small amount (5 wt%) of SP or CNTs as the conductive additive during the slurry-making process. For the SP case (Figure 1g–h, Figure S3a–c, Supporting Information), the LRCs active materials were surrounded by SP additives. For the CNTs (Figure 1i, Figure S3d–f, Supporting Information), we cannot see the primary particles of LRCs as they have been completely coated by the CNTs additive. More importantly, the LRCs particles are connected by CNTs, forming a conductive network for the entire electrode. It can be predicted that such an integral conductive network combined with the high intrinsic conductivity of CNTs will be conducive to the rate performance of LRCs.

2.2. Redox Mechanism of LRCs

Charge curves in Figure 2a display the typical two-step charge profiles of LRCs, with a slope at relatively low potential (<4.4 V), and a long platform at approximately 4.5 V. Ex situ X-ray photoelectron spectroscopy (XPS) profiles were collected initially and at 4.4 V and 4.8 V are used to reveal the redox mechanism of LRCs in the slope and platform region, respectively. The O 1s XPS profiles usually show multi-peak overlap in the LIBs field due to the various origins of the O signal, mainly including the

lattice O from active materials and inorganic (Li₂CO₃, Li₂O) and organic (LiCH₂CH₂OCO₂Li) O species from the SEI.^[22,23] Therefore, the deconvolution of the O XPS profiles should be conducted very carefully, and we use the minimum number of components, unless it is impossible to properly fit the spectra without it.^[24]

From the O XPS profiles in Figure 2b, the gray peaks at approximately 531.3 and 533 eV can be indexed to surface deposits such as adsorptive oxygen and SEI, but they are not the focus of this work. The O XPS patterns at the initial and 4.4 V stage exhibit a similar profile, with only a lattice O²⁻ (blue peak, ≈529.4 eV), demonstrating that the lattice oxygen has not been oxidized in the slope region. Nevertheless, a new red peak at a higher binding energy (≈530.8 eV) appears when the LRCs is further charged to 4.8 V, revealing the oxidized lattice oxygen during the platform region.

From the Mn XPS profiles in Figure 2c, the blue and red peaks at approximately 643.3 and 654.8 eV can be assigned to the Mn 2p_{2/3} and Mn 2p_{1/3} signals, respectively. Both these peaks move to a slightly higher binding energy from the initial stage to 4.4 V, and maintain their position until 4.8 V, indicating that the Mn element is only oxidized during the slope region rather than the platform region. However, the weak Ni 2p and Co 2p XPS profiles (Figure S5, Supporting Information) cannot be used to further support the redox mechanism of the transition metal, owing to the low content of Ni and Co in the LRCs.

Overall, the slope at a relatively low potential (<4.4 V) and the long platform at approximately 4.5 V can be attributed to transition metal and oxygen redox reactions, respectively. The structural evolution of LRCs during the first cycle can also be obtained from the Supporting Information based on ex situ XRD and Raman patterns (Figures S6–S7, Supporting Information).

2.3. O-redox Kinetics Revealed by GITT

The O-redox kinetics of Li⁺ diffusion in a solid electrode was first revealed using the GITT. The GITT in this work (Figure 3a) applied a pulse current of 0.1 C (1C = 300 mAh g⁻¹) for 1 h, with a 10 h interruption between each pulse, and a total of 12 points were collected to measure open circuit (OCV) voltage, time constant, and impedance. The two typical OCV curves inserted in Figure 3a show that the voltage at point 3 (blue) can quickly reach the equilibrium state, whereas the OCV at point 10 (red) appears as a never-ending voltage relaxation process, indicating fast and sluggish kinetics during the transition metal and oxygen redox of LRCs, respectively. From Figure 3b, both the SP and CNTs cases exhibit relatively small ΔOCV from points 1 to 4, whereas large ΔOCV from points 5 to 12, in agreement with the conclusion obtained from Figure 3a. Meanwhile, ΔOCV in the slope region for SP and CNTs is almost the same, but CNTs display clearly lower ΔOCV than SP in the platform region, demonstrating that the CNTs conductive additives mainly accelerate the O-redox of LRCs.

The time constant (D/R^2), rather than the diffusion coefficient (D), was used in this work to further evaluate the O-redox kinetics to eliminate the error caused by measuring the particle size (R) of LRCs based on SEM images.^[25] The

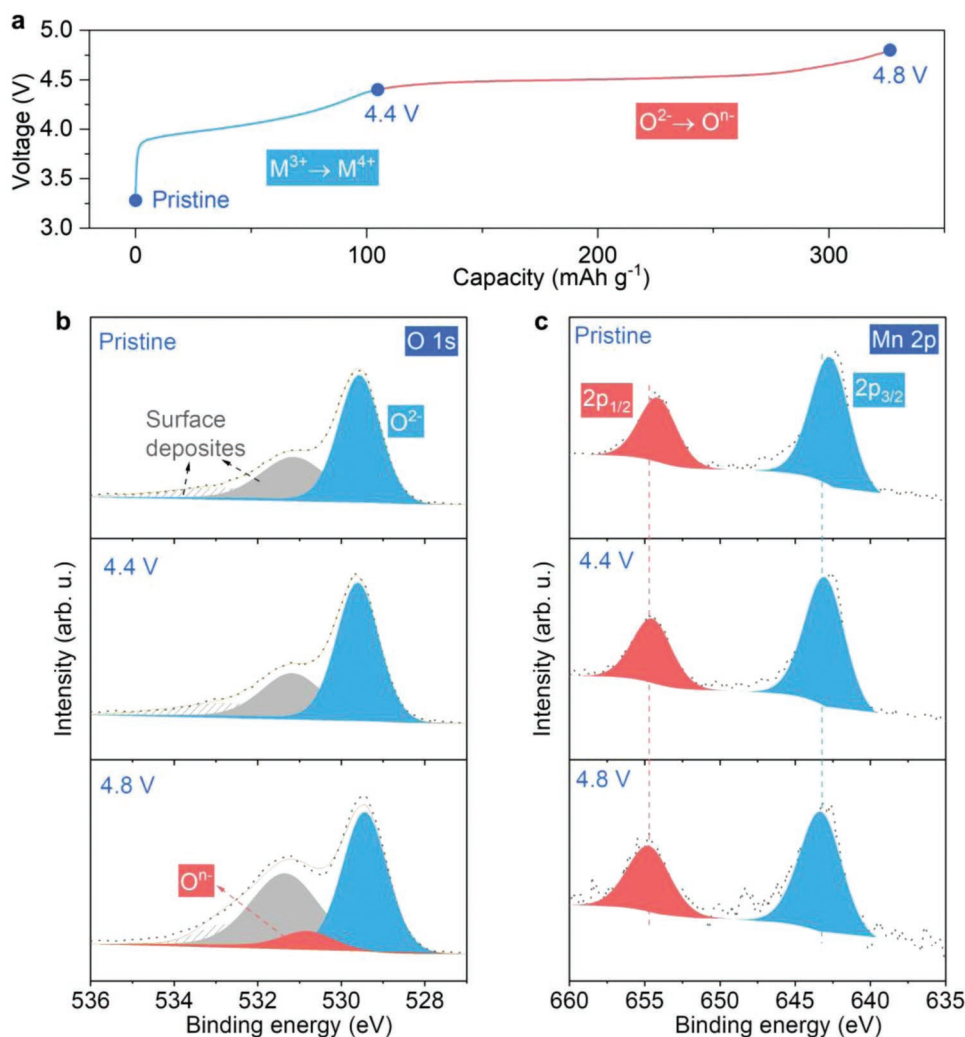


Figure 2. Redox mechanism of LRCs. a) The initial charge curves of LRCs. b–c) Ex situ O 1s (b) and Mn 2p (c) XPS profiles of the LRCs electrode collected at special status based on (a).

time constant (Figure 3c) can be calculated using the equation

$$D/R^2 = \frac{1}{9It} \left(\frac{\Delta E_s}{\Delta E_t} \right)^2$$

where t , ΔE_s , and ΔE_t represent the pulse time and voltage variation during the relaxation and pulse processes, respectively (see Supporting Information for more details, Figure S8, Supporting Information). In Figure 3d, the D/R^2 values in the initial four points are much larger than that in the last eight points, and the CNTs display a slightly larger value than SP, again demonstrating that CNTs can effectively improve the sluggish kinetics of the O-redox reaction.

2.4. O-Redox Kinetics Revealed by EIS

The O-redox kinetics of the interface and charge transfer impedance were revealed using EIS. There are usually four parts in Nyquist plots: an intercept with the x -axis at ultrahigh frequency represents the impedance of the electrolyte (R_e), a semi-circle at high frequency (HF) represents the impedance of the interface contact such as SEI (R_{SEI}), a semi-circle

at middle frequency (MF) represents the impedance of charge transfer (R_{ct}), and a slope at low frequency (LF) represents solid diffusion (Z_W). The corresponding equivalent circuit and Li^+ diffusion paths are shown in Figure 4a,b to better understand these processes. The solid diffusion of Li^+ (Z_W) was explored by GITT in the previous section, and R_e remained almost the same in this work. Therefore, the focus of this section is on the R_{SEI} and R_{ct} .

Ex situ Nyquist plots collected during the voltage relaxation process of the GITT (the previous section) are shown in Figure 4c,d for the SP and CNTs cases, respectively. Both SP and CNTs exhibit a four-part EIS nature, and each part is separated by cyan and light-blue dots. The R_{SEI} statistics in Figure 4e show relatively low impedance for the initial four points and high impedance for the remaining eight points. This is because the O-redox region produces species with strong oxidizability, such as O^- and O_2^{2-} , resulting in the decomposition of the electrolyte and increased impedance of the SEI. Meanwhile, the R_{SEI} of CNTs was higher than that of SP owing to its larger specific surface area. For R_{ct} in Figure 4e, the SP and CNTs show

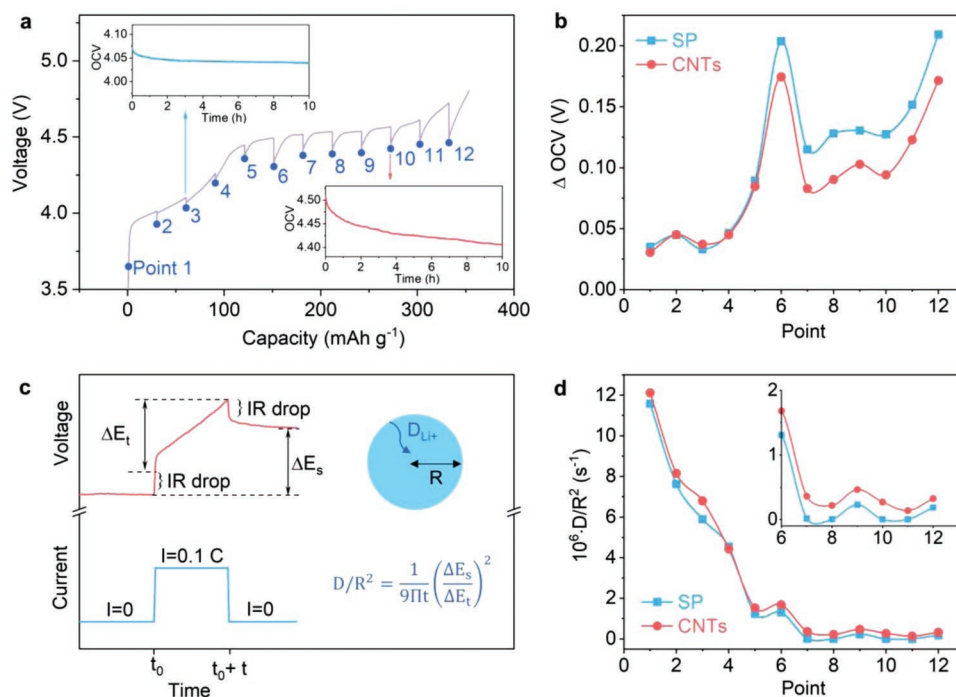


Figure 3. Kinetics characterization of LRCs with SP and CNTs by GITT. a) The initial charge GITT curves (1 h, 0.1 C pulse, 10 h rest, 1C = 300 mAh g⁻¹) of LRCs with the insets show two typical OCV curves at slope and platform regions, respectively. b) Δ OCV values of LRCs electrode with SP and CNTs additives. c) A typical part of enlarged GITT profiles shows its current and voltage variation with the insets displaying the equation of calculating the time constant (D/R^2). (d) D/R^2 values of the LRCs electrode with SP and CNTs additives.

a “concave-shape” change trend, which consists of the classical intercalation mechanism. The enlarged patterns in Figure 4e further reveal that CNTs can accelerate both cationic and anionic redox reactions. The GITT and EIS profiles during the discharge process are also presented in the Supporting Information (Figure S9–S10, Supporting Information).

2.5. Electrochemical Performance of LRCs

The electrochemical performance of LRCs with SP or CNTs was tested using a 2025-type coin cell. From the initial charge–discharge curves at various C-rates (Figure 5a–c), SP and CNTs show similar profiles at low current densities (0.1 C), whereas the CNTs exhibit much smaller voltage polarization than SP at higher C-rates (1 C and 2 C), indicating accelerated kinetics. The specific capacity statistics from cationic (M-redox, < 4.4 V) and anionic redox (O-redox, 4.4–4.8 V) are shown in Figure 5d. With the introduction of CNTs as a conductive additive, the capacities arising from the O-redox were obviously improved, especially at high C-rates.

The long cycling performance at a relatively high C-rate (2 C) is further presented in Figure 5e. The CNTs showed desirable cycling performance with respect to capacity retention (89%) and coulombic efficiency (Figure S11, Supporting Information, average value: 99.4%) for over 200 cycles. The slight capacity increase in the initial 20 cycles can contribute to the typical activation of the Li₂MnO₃ compound and the special charge/discharge protocol in this work without using small-current formation cycles.^[26] Meanwhile, a sudden capacity jump at

special cycles is caused by temperature variation. However, for the SP case, it can only normally cycle for approximately 70 cycles with poor coulombic efficiency (Figure S12, Supporting Information).

Detailed charge/discharge curves at various cycles are shown in Figure 5f–g to reveal the reasons for the capacity and voltage decay during long cycling. By comparing the profiles between the 2nd and 50th cycles of CNTs, a capacity increase and a strange charge voltage drop can be observed. This indicates the unique surface structure reconstruction of LRCs rather than a typical voltage polarization because pure polarization can cause a charge voltage increase.^[15] During the following cycling, CNTs delivered a relatively small capacity and voltage fade compared with the SP case. From the EIS profiles after 200 cycles (Figure 5h), SP exhibits a similar R_{SEI} but much higher R_{ct} compared to CNTs, further demonstrating that CNTs can improve the capacity retention of LRCs by increasing its kinetics.

2.6. Failure Mechanism of LRCs

Coin cells based on SP or CNTs after cycling were disassembled to elucidate the failure mechanism of LRCs in terms of bulk and surface evolution. From SEM images in Figure 6a–b, the conductive networks for the CNTs case remained in place, in agreement with its lower impedance after 100 cycles. For the XRD patterns in Figure 6c, the (003) peak for both SP and CNTs shifted to a smaller angle compared to the initial LRCs, revealing their expanded interlayer spacing along the *c*-axis. Meanwhile, the Bragg intensity of SP was

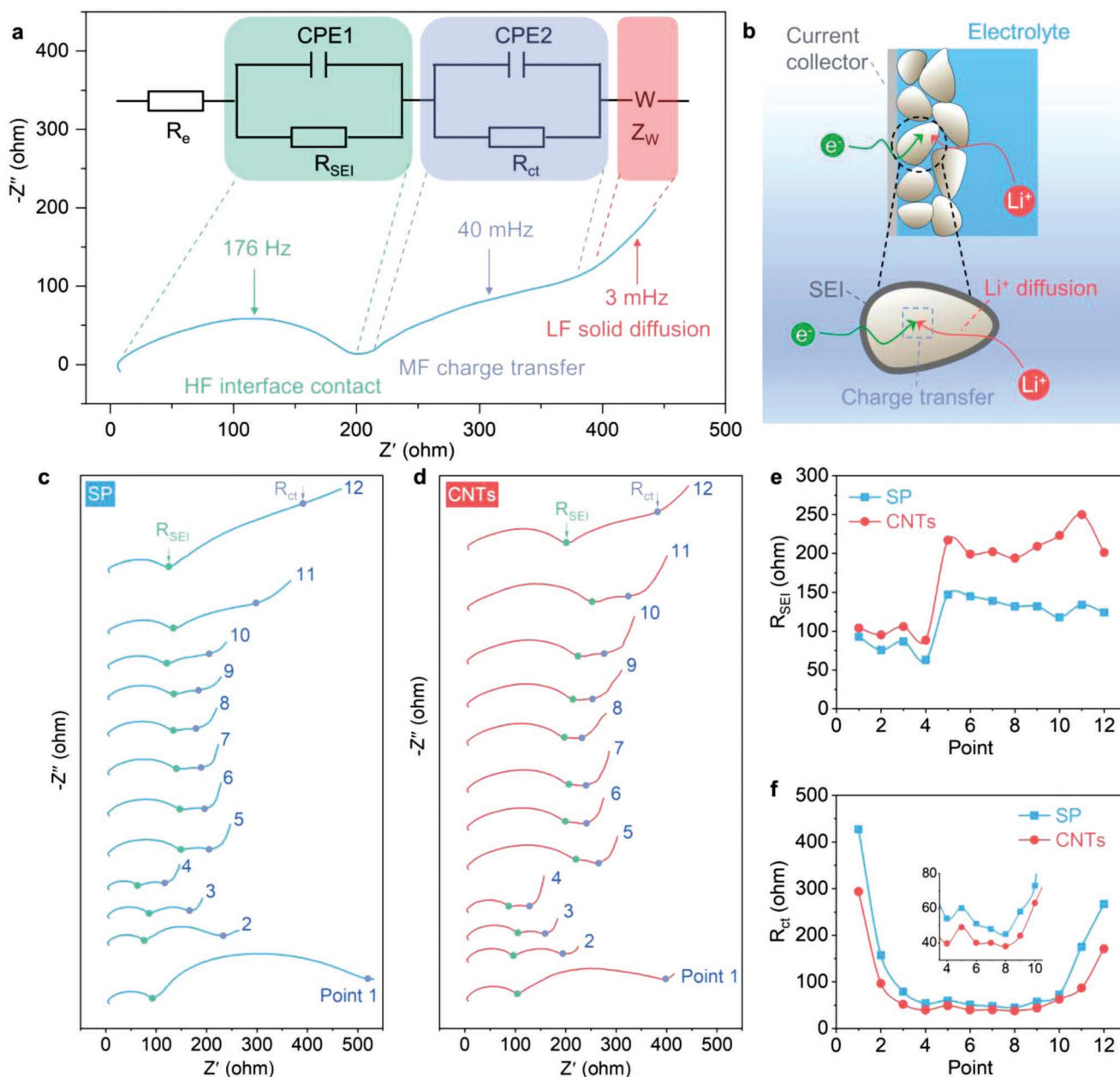


Figure 4. Kinetics characterization of LRCs with SP and CNTs by EIS. a) A typical Nyquist curve and corresponding equivalent circuit of LRCs. b) A common schematic about how Li^+ and electron diffuse in LIBs. c–d) Ex situ EIS profiles of LRCs with SP (c) and CNTs (d). e–f) R_{SEI} (e) and R_{ct} (f) of LRCs with SP and CNTs based on the Nyquist curves in (c–d).

slightly lower than that of CNTs, indicating that it had more structural defects after cycling. From the Raman spectra in Figure 6d, the two strongest Raman peaks at about 601 cm^{-1} and 586 cm^{-1} can be assigned to the A_{1g} (M–O stretching, M represents transition metal) and E_g (O–M–O bending) mode of NMC ($\text{LiNi}_x\text{Co}_y\text{Mn}_{1-x-y}\text{O}_2$) in LRCs. Moreover, the shoulder peaks at around 430 cm^{-1} and 663 cm^{-1} can be indexed to Li_2MnO_3 in the LRCs as well as the distorted spinel-like structure, respectively.^[27] The much stronger NMC and Li_2MnO_3 peaks of CNTs case compared to those of SP indicate its better structural stability after cycling.

The surface structure evolution of LRCs with SP or CNTs will be detected by electron energy loss spectroscopy (EELS) of the O–K and Mn–L edges. The O pre-peak at approximately 532.8 eV can be assigned to the transition of the O-1s core state to the unoccupied O-2p states hybridized with M-3d states.^[27–31] The disappearance of the O pre-peak for the SP case at the surface (blue spectra, Figure 6e) indicates the nature of its oxygen loss. From Figure S17, Supporting Information, the Mn-L edges for both SP and CNTs shift to a lower energy at the surface compared to the bulk, revealing their reduced oxidation state at the surface. This result is consistent with the capacity activation

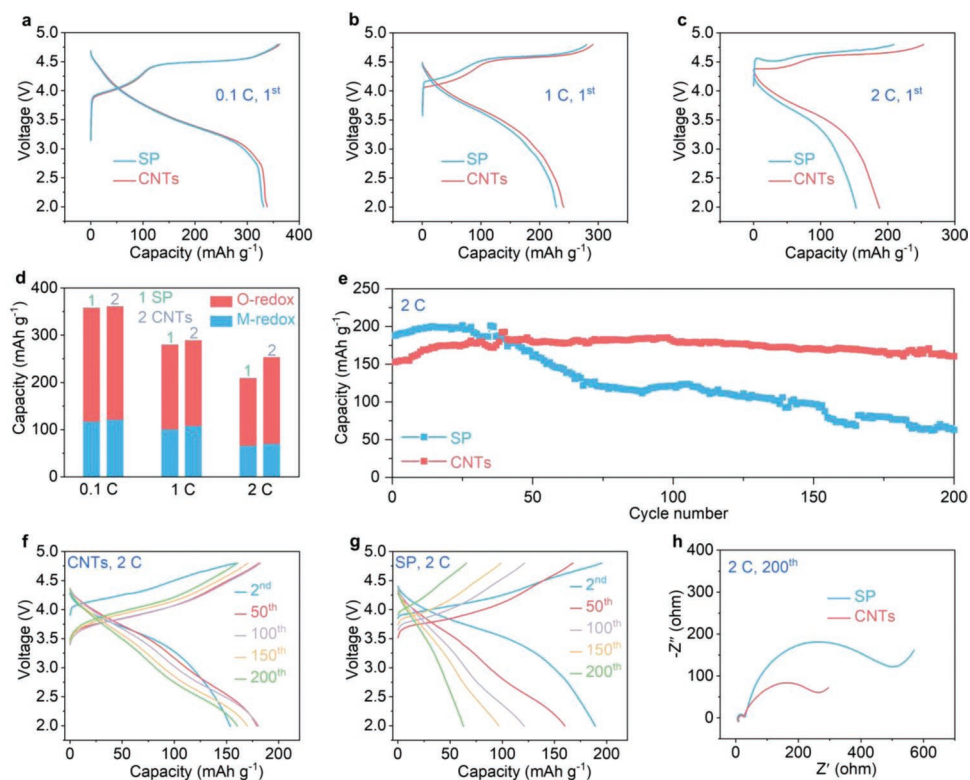


Figure 5. Electrochemical properties of LRCs using SP and CNTs. a) The initial charge–discharge curves at a) 0.1 C, b) 1 C, and c) 2 C. d) Capacity contribution statistics from cationic and anionic redox. e) Long cycling performance at 2 C. f–g) Charge–discharge curves of LRCs with SP (f) and CNTs (g) at various cycles. h) EIS patterns of LRCs after 200 cycles.

of LRCs mentioned above, and the valence variation is caused by the typical surface evolution of LRCs from a layer to spinel structure.^[15] Overall, LRCs with CNTs exhibit a relatively more stable bulk and surface structure than LRCs with SP during cycling, resulting in better cycling stability.

3. Conclusions

We constructed a complete conductive network by simply introducing a small amount of CNTs additives during the slurry-making process to improve the poor kinetics of the LRCs. Ex situ XPS demonstrates the separate cationic and anionic redox of LRCs during the initial charge process; that is, the slope at a relatively low potential and long platform at approximately 4.5 V can be attributed to the transition metal and oxygen redox, respectively. The combination of GITT and EIS revealed that the battery with CNTs showed a lower Δ OCV, larger time constant, and smaller impedance than that with SP, delivering accelerated kinetics, particularly for the O-redox process. Consequently, the LRCs with CNTs exhibits a much better rate and cycling performance (\approx 89% capacity retention at 2C for over 200 cycles) than the SP case. Eventually, TEM results imply that the improved electrochemical performance of the CNTs case also benefits from its more stable bulk and surface structures. Such a facile conductive additive modification strategy also provides a universal approach to enhance the electron diffusion properties of other electrode materials, such as LiFePO_4 , Si, and S.

4. Experimental Section

Electrode Preparation: The LRCs electrodes were prepared by first mixing commercial $\text{Li}_{1.2}\text{Mn}_{0.54}\text{Ni}_{0.13}\text{Co}_{0.13}\text{O}_2$ (Guangdong Canrd Corporation) as active materials, Super P (TIMCAL) or CNTs (Guangdong Canrd Corporation, dispersed in NMP solvent with a solid content of 4 wt%) as conductive additives, and poly(vinylidene fluoride) (PVDF, Arkema) as a binder at a mass ratio of 90: 5: 5 in N-methylpyrrolidone (NMP, Aladdin) solvent by magnetic stirring for 12 h. The obtained slurry was cast on an Al foil with a thickness of 200 μm using a scraper and dried at 80 °C for 2 h. Subsequently, the electrode was cut into disks (diameter = 14 cm) with an active material loading of approximately 4 mg cm^{-2} (thickness of approximately 50 μm). Subsequently, it was further dried at 110 °C for 8 h in a vacuum oven before being transferred into a glove box.

Battery Assembly: Li- LRCs 2025-type coin cells were assembled in a glove box with the LRCs work electrode, a Li metal disk counter electrode (diameter = 1.5 cm, thickness = 0.3 mm, Alfa Aesar, 99.9%), a Celgard 2325 separator, and 1 M LiPF_6 in EC-DMC-DEC (1:1:1 by volume) as the electrolyte (\approx 80 μL).

Electrochemical Measurements: Cycling and rate performance at 0.1, 0.5, 1, 2, and 5 C (1 C = 300 mA g^{-1}) between 2–4.8 V (versus Li/Li⁺) were tested at 25 °C using a CT3001A system (Wuhan LAND). Electrochemical impedance spectroscopy (EIS) was performed between 1 000 000 and 0.001 Hz with a bias voltage of 0.005 V using a CHI800D system (CH Instruments).

XRD Measurements: All XRD patterns were obtained using a Bruker D8 Advance diffractometer with a Cu K α radiation source operating at 40 kV and 40 mA. For failure analysis, coin cells after cycling were first disassembled in a glove box to obtain the working electrode, which was then washed with DMC to remove the remaining electrolyte and dried at room temperature. The dried electrode was then sealed on

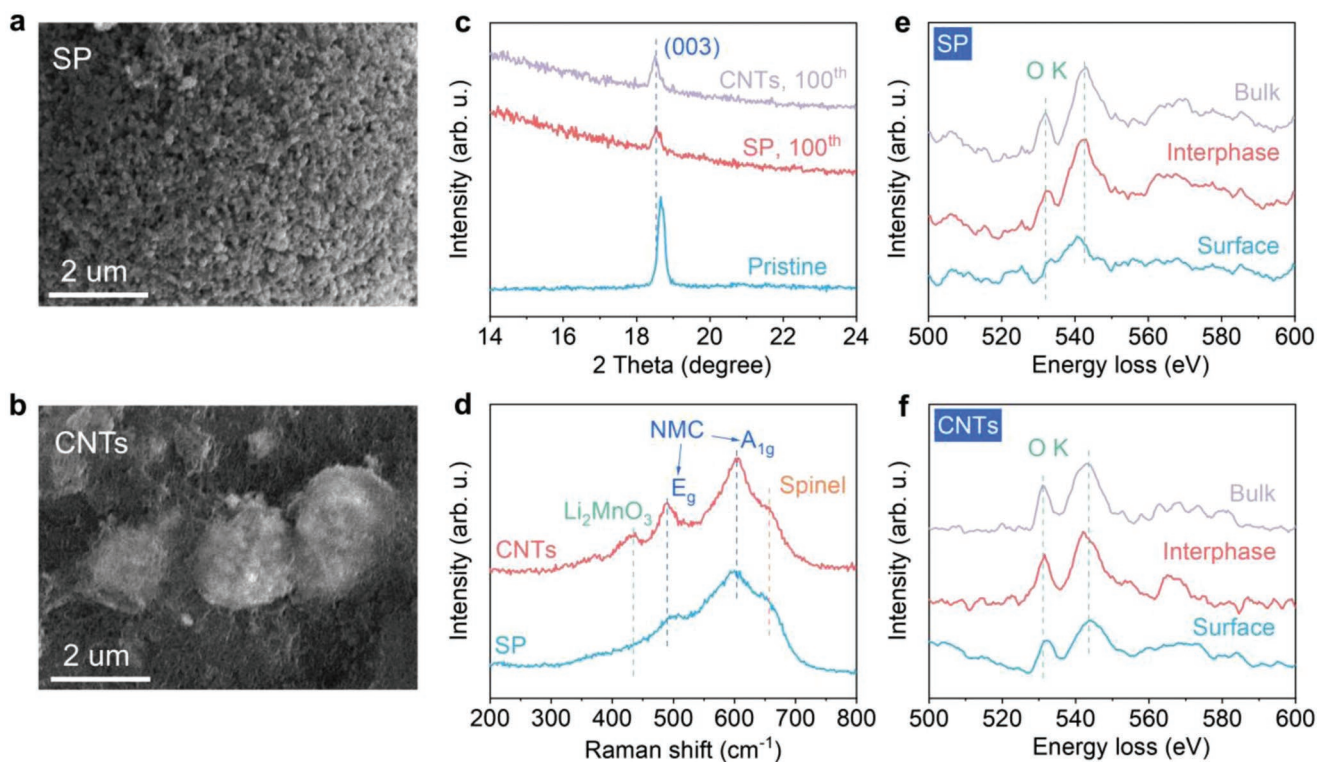


Figure 6. Physical characterization of the LRCs with SP and CNTs after 100 cycles. a–b) SEM images. c–d) XRD and Raman patterns. e–f) O-K edges EELS.

the XRD specimen stage using polyimide tape to avoid contact with the air.

Raman Measurement: After cycling in the glove box, the dried electrode was first fixed on a microslide to avoid contact with air. Raman spectra were obtained using a micro-Raman spectrometer (Horiba Jobin Yvon, HR Evolution) using a neon laser with a wavelength of 532 nm.

SEM Measurement: After cycling in the glove box, the dried electrode was first fixed on the SEM specimen stage and sealed with a special setup to avoid contact with air. SEM images were obtained using a Hitachi SU8010 SEM operating at 10 kV and 10 mA.

XPS Measurement: The dried electrode after cycling in the glove box was first fixed on an XPS specimen stage and then placed in a vacuum transfer chamber to avoid contact with air. X-ray photoelectron spectroscopy (XPS) patterns were obtained using a Thermo Fisher Escalab 250Xi XPS instrument with an Al K α radiation source. All binding energies in this study were calibrated based on C contamination with the C1s peak at 284.4 eV.

TEM Measurements: LRCs powders were first dissolved in ethyl alcohol, and then the dispersion was dripped onto a standard Cu grid and dried at room temperature. The TEM, HAADF-STEM, EDS, and EELS profiles were obtained using a spherical aberration-corrected FEI Titan Themis Cubed G2 300 TEM operating at 300 kV. CNTs and SP were tested at 80 kV to avoid electron irradiation.

Statistical Analysis: All results including spectra, images, and electrochemical data presented in this work were repeated at least three times. Specifically, the mean sample size driven from SEM images was obtained by using the “Nano Measure 1.2” statistical software. The electrochemical data in this paper was the mean value of three repeated data with desirable consistency. For the deconvolution of the O XPS profiles, we use the minimum number of peaks, unless it is impossible to properly fit the spectra without it. For the O-K edge EELS, background correction was conducted for obtaining higher signal to noise ratio spectra.

Supporting Information

Supporting Information is available from the Wiley Online Library or from the author.

Acknowledgements

J.Z. and Z.C. contributed equally to this work. This work was supported by the National Natural Science Foundation of China (Grant Nos. 52071225), the Czech Republic from ERDF “Institute of Environmental Technology – Excellent Research” (No. CZ.02.1.01/0.0/0.0/16_019/0000853). M.H.R. thanks the Sino-German Research Institute for their support (Project GZ 1400). J.H.C. would like to thank the National Natural Science Foundation of China (Grant No. 11874044). J.Y.S. thanks the National Natural Science Foundation of China (51702225), the Beijing Municipal Science and Technology Commission (Z161100002116020), and the Natural Science Foundation of Jiangsu Province (BK20170336). R.Z.Y. thanks the National Natural Science Foundation of China (Grant nos. 51972220 and 51572181), the National Key Research and Development Program of China (2016YFB0100200), and the Key University Science Research Project of Jiangsu Province (No. 20KJA480003).

Open access funding enabled and organized by Projekt DEAL.

Conflict of Interest

The authors declare no conflict of interest.

Data Availability Statement

Research data are not shared.

Keywords

accelerated O-redox kinetics, CNTs, conductive additives, lithium-rich cathode

Received: April 7, 2022

Revised: May 5, 2022

Published online: May 19, 2022

- [1] D. Larcher, J. M. Tarascon, *Nat. Chem.* **2015**, *7*, 19.
- [2] J. B. Goodenough, Y. Kim, *Chem. Mater.* **2009**, *22*, 587.
- [3] B. You, Z. Wang, F. Shen, Y. Chang, W. Peng, X. Li, H. Guo, Q. Hu, C. Deng, S. Yang, G. Yan, J. Wang, *Small Methods* **2021**, *5*, 2100234.
- [4] J. B. Goodenough, K. S. Park, *J. Am. Chem. Soc.* **2013**, *135*, 1167.
- [5] C. Xu, K. Marker, J. Lee, A. Mahadevegowda, P. J. Reeves, S. J. Day, M. F. Groh, S. P. Emge, C. Ducati, B. L. Mehdi, C. C. Tang, C. P. Grey, *Nat. Mater.* **2021**, *20*, 84.
- [6] W. Li, X. Liu, H. Celio, P. Smith, A. Dolocan, M. Chi, A. Manthiram, *Adv. Energy Mater.* **2018**, *8*, 1703154.
- [7] G. Assat, J.-M. Tarascon, *Nat. Energy* **2018**, *3*, 373.
- [8] J. Xu, M. Sun, R. Qiao, S. E. Renfrew, L. Ma, T. Wu, S. Hwang, D. Nordlund, D. Su, K. Amine, J. Lu, B. D. McCloskey, W. Yang, W. Tong, *Nat. Commun.* **2018**, *9*, 947.
- [9] P. M. Csernica, S. S. Kalirai, W. E. Gent, K. Lim, Y.-S. Yu, Y. Liu, S.-J. Ahn, E. Kaeli, X. Xu, K. H. Stone, A. F. Marshall, R. Sinclair, D. A. Shapiro, M. F. Toney, W. C. Chueh, *Nat. Energy* **2021**, *6*, 642.
- [10] R. A. House, J.-J. Marie, M. A. Pérez-Osorio, G. J. Rees, E. Boivin, P. G. Bruce, *Nat. Energy* **2021**, *6*, 781.
- [11] R. A. House, G. J. Rees, M. A. Pérez-Osorio, J.-J. Marie, E. Boivin, A. W. Robertson, A. Nag, M. Garcia-Fernandez, K.-J. Zhou, P. G. Bruce, *Nat. Energy* **2020**, *5*, 777.
- [12] M. B. Yahia, J. Vergnet, M. Saubanere, M. L. Doublet, *Nat. Mater.* **2019**, *18*, 496.
- [13] X. Yu, Y. Lyu, L. Gu, H. Wu, S.-M. Bak, Y. Zhou, K. Amine, S. N. Ehrlich, H. Li, K.-W. Nam, X.-Q. Yang, *Adv. Energy Mater.* **2014**, *4*, 1300950.
- [14] Y.-N. Zhou, J.-L. Yue, E. Hu, H. Li, L. Gu, K.-W. Nam, S.-M. Bak, X. Yu, J. Liu, J. Bai, E. Dooryhee, Z.-W. Fu, X.-Q. Yang, *Adv. Energy Mater.* **2016**, *6*, 1600597.
- [15] J. Zheng, P. Xu, M. Gu, J. Xiao, N. D. Browning, P. Yan, C. Wang, J.-G. Zhang, *Chem. Mater.* **2015**, *27*, 1381.
- [16] J. Hong, W. E. Gent, P. Xiao, K. Lim, D. H. Seo, J. Wu, P. M. Csernica, C. J. Takacs, D. Nordlund, C. J. Sun, K. H. Stone, D. Passarello, W. Yang, D. Prendergast, G. Ceder, M. F. Toney, W. C. Chueh, *Nat. Mater.* **2019**, *18*, 256.
- [17] S. Liu, L. Kang, S. C. Jun, *Adv. Mater.* **2021**, *33*, 2004689.
- [18] P. Oh, M. Ko, S. Myeong, Y. Kim, J. Cho, *Adv. Energy Mater.* **2014**, *4*, 1400631.
- [19] Y. Wang, Z. Yang, Y. Qian, L. Gu, H. Zhou, *Adv. Mater.* **2015**, *27*, 3915.
- [20] S. Liu, Z. Liu, X. Shen, W. Li, Y. Gao, M. N. Banis, M. Li, K. Chen, L. Zhu, R. Yu, Z. Wang, X. Sun, G. Lu, Q. Kong, X. Bai, L. Chen, *Adv. Energy Mater.* **2018**, *8*, 1802105.
- [21] A. C. Ferrari, D. M. Basko, *Nat. Nanotechnol.* **2013**, *8*, 235.
- [22] S. Jiao, X. Ren, R. Cao, M. H. Engelhard, Y. Liu, D. Hu, D. Mei, J. Zheng, W. Zhao, Q. Li, N. Liu, B. D. Adams, C. Ma, J. Liu, J.-G. Zhang, W. Xu, *Nat. Energy* **2018**, *3*, 739.
- [23] J. Zheng, M. H. Engelhard, D. Mei, S. Jiao, B. J. Polzin, J.-G. Zhang, W. Xu, *Nat. Energy* **2017**, *2*, 17012.
- [24] G. Assat, D. Foix, C. Delacourt, A. Iadecola, R. Dedryvere, J. M. Tarascon, *Nat. Commun.* **2017**, *8*, 2219.
- [25] G. Assat, C. Delacourt, D. A. D. Corte, J.-M. Tarascon, *J. Electrochem. Soc.* **2016**, *163*, A2965.
- [26] D. Ye, G. Zeng, K. Nogita, K. Ozawa, M. Hankel, D. J. Searles, L. Wang, *Adv. Funct. Mater.* **2015**, *25*, 7488.
- [27] J. Zhou, X. Lian, Q. Shi, Y. Liu, X. Yang, A. Bachmatiuk, L. Liu, J. Sun, R. Yang, J.-H. Choi, M. H. Rummeli, *Adv. Energy Sustainability Res.* **2021**, *3*, 2100140.
- [28] B. Xu, C. R. Fell, M. Chi, Y. S. Meng, *Energy Environ. Sci.* **2011**, *4*, 2223.
- [29] J. Liu, J. Wang, Y. Ni, Y. Zhang, J. Luo, F. Cheng, J. Chen, *Small Methods* **2019**, *3*, 1900350.
- [30] S. Liu, L. Kang, J. Zhang, E. Jung, S. Lee, S. C. Jun, *Energy Storage Mater.* **2020**, *32*, 167.
- [31] S. Liu, L. Kang, J. Hu, E. Jung, J. Zhang, S. C. Jun, Y. Yamauchi, *ACS Energy Lett.* **2021**, *6*, 3011.